Laser surface polishing of Ti-6Al-4V parts manufactured by laser powder bed fusion

**Muhannad Ahmed Obeidi[1,2,3, a, ∗], Andre Mussatto[1,2,3, a], Merve Nur Dogu[1,2,3],
Sithara P. Sreenilayam[1,2,3], Eanna McCarthy[1,2,3], Inam Ul Ahad[1,2,3],
Shane Keaveney[4], Dermot Brabazon[1,2,3]**

[1]I-Form Advanced Manufacturing Research Centre, Dublin City University, Dublin, Ireland
[2]School of Mechanical & Manufacturing Engineering, Dublin City University, Dublin, Ireland
[3]Advanced Processing Technology Research Centre, Dublin City University, Dublin, Ireland
[4]Croom Precision Medical, Croom, Co. Limerick, Ireland

[a] The authors have made an equal contribution to the article

*Corresponding author: muhannad.ahmedobeidi@dcu.ie

Abstract

Poor surface quality of Additively Manufactured (AM) components, can greatly increase the overall cost and lead time of high-performance components. Examples are medical devices where surfaces may contact the patient's skin and hence need to be smooth and aerospace components with high fatigue strength requirements where surface roughness could reduce fatigue life. The average surface roughness (Ra) of AM parts can reach high levels greater than 50 microns and maximum distance between the high peaks and the low valleys of more than 300 microns. As such, there is a need for fast, cost effective and selective finishing methods of AM produced components targeted at high-performance industries. In this paper Ti-6Al-4V Grade 23 ELI, popular for medical devices and aerospace parts production, was L-PBF processed to manufacture parts which were subsequently treated via laser polishing. Here in this work, CO_2 laser polishing was used for the surface modification of the Ti-6Al-4V produced samples. The most significant processing parameters were optimised to achieve approximately an 80% reduction in the average surface roughness and a 90% reduction in the peak-to-valley distance with a processing time of 0.1 sec/mm^2 and cost of 0.2 €/cm^2.

Keywords: Laser polishing, Ti-6Al-4V, Powder bed fusion, Biomedical application, Additive manufacturing, Surface profile roughness

1. Introduction

Ti-6Al-4V (also known as α+β type titanium (Ti) alloy or Ti64) parts can be produced by using the traditional manufacturing techniques (*e.g.,* casting, forging, and bulk feedstock material rolling) followed by machining to obtain the desired dimension and shape [1,2]. However, these conventional processes always lead to high production costs, longer timelines and results in large materials wastage and tool wear. In recent years, additive manufacturing (AM) of complex Ti-6Al-4V geometries has received much attention [3]. AM methods allow the fabrication of complicated high-quality elements and customized biomedical devices that are challenging if not impossible to be manufactured by other methods [4–11]. Additively manufactured Ti-6Al-4V based porous orthopaedic implants have been developed using selective electron beam melting (EBM) [12], laser powder bed fusion (L-PBF) [13], and laser metal deposition (LMD) [14] techniques. Hollander *et al.* [15]developed several implants such as porous cylinder and human vertebra models by direct laser forming of Ti-6Al-4V powder with a particle size of 25–45 μm. Murr *et al.* [16] studied porous AM Ti-6Al-4V implants fabricated

using L-PFB and examined *via* micro-CT scan. The performance of the biomedical implants depends on both bulk material characteristics which meet the mechanical necessities and surface properties that strongly affect bio-integration.

Ti-6Al-4V alloy has microstructure with body-centred cubic (β-phase) and closed packed hexagonal crystal (α-phase), is the most popular and first practical Ti alloy synthesised originally in 1950s [17]. It has been widely used for applications in complex industrial components developments due to its excellent physical, chemical and mechanical properties [18,19]. In this α+β material type, the room temperature stable α-phase transforms to β-phase at approximately 1000 °C, that depends on the oxygen (O) and aluminium (Al) content [20]. Several studies have found that the formation of different microstructures under thermomechanical or thermal cycles strongly affects its properties such as ductility, wear resistance, strength, hardness, corrosion behaviour, fatigue, and toughness [21,22]. Therefore, by achieving a suitable microstructure, the mechanical properties can be tailored for a specific application. Ti-6Al-4V exhibits high corrosion resistance, low density, high specific strength, and high fracture toughness [23,24]. This advanced light weight material (*i.e.* ~60% lower density than that of steel based materials) is still in high demand in the aerospace industry [25,26]. Due to exceptional corrosion resistance to most alkalis and acids, it has been used extensively in chemical, and marine industries in the past few decades [27]. All its outstanding properties combined with excellent biocompatibility with human tissues and Osseo integration in contact with human bone make Ti-6Al-4V attractive in biomedical device applications (*e.g.*, dental and orthopaedic implant) [28] . In particular, the non-ferromagnetic nature of this material allows safer medical examination using magnetic resonance imaging (MRI) and, hence it is suitable for long-term usable biomedical implants fabrication. Some other application areas of Ti-6Al-4V are in electronics, sports, transport, as well as oil and gas extraction [29].

Ti-6Al-4V components fabricate *via* L-PBF usually exhibit high roughness *i.e.*, the average surface roughness (Ra) ranging from 5 µm - 20 µm. This low level of surface dimension precision can lead to large degree of friction in mating surfaces and a reduce therapeutic effect in biomedical implants [30]. Surface finishing of orthopaedic and dental implants is vital in order to achieve a hygienic sterilize surface with good bio-integration properties. Despite precautions, the implant surface can see bacterial growth, setting off bacterial infection. However, the bacterial adhesion or growth can be prevented by improving surface finish as the bacterial attachment enhances only when the surface features have dimensions similar to the size of the bacteria [31]. The traditional surface polishing gives the surface roughness value ~ 0.3–0.6 µm in mechanical polishing, < 1 µm *via* chemical polishing and <10 nm in electrolytic polishing [32]. However, all these traditional finishing processes of AM parts show many drawbacks including low efficiency, being time-consuming, and having a chemical risk, limiting their clinical application. Studies show that recently developed emerging cost-effective and high-speed Laser Polishing (LP) methods involving ablation and melting of thin substrate materials *via* laser irradiation offers improved surface quality and enhanced mechanical properties [33–37]. Here, the input thermal energy is one of the vital parameters that affects significantly the melt pool convection and thereby the quality of surface. In this process, the metal surface solidifies without pores, cracks, or hidden surface defects out of the molten material. When it re-melts, the initial surface roughness is smoothed by the melt pool surface tension. In most studies, LP of the metal surface is performed with a continuous wave or pulsed laser beam at constant average laser power, or intensity. Several studies have been reported on the laser surface modification of Ti-6Al-4V parts. Ma *et al.*[38]*,* reported the reduction of surface roughness of an AM Ti-6Al-4V component from 5µm to 1µm using a nanosecond pulsed fiber laser having wavelength 1060 nm. In another study, Liang *et al.*[39] reported the surface polishing of a Ti-6Al-4V implant using a nanosecond pulsed fiber laser and the improved value Ra 2.1 µm. The implants were manufactured *via* L-PBF using Ti-6Al-4V powder having density 4.41 g/cm^3 and Ra 10.2 µm. Marimuthu *et al.*

[40] optimised laser processing parameters to polish SLM produced Ti–6Al–4V samples using a continuous wave fiber laser at 1070–1090 nm wavelength and able to achieve 2.44 μm surface roughness from the initial Ra ~10.2 μm by controlling the laser power, speed and beam offset. They investigated the chemical composition of the samples and found similar EDX results before and after the laser polishing. Controlled surface asperity is critical for bioimplants to achieve the desired tribological performance. Poor surface integrity and wear characteristics of bioimplants could result in release of material in the body and could lead to mechanical failure [41]. Kutsukake *et al.* [42] investigated the influence of surface roughness on the osteoinductivity of polished and unpolished L-PBF produced Ti-6Al-4V implants in rat femur bone. They demonstrated that new bone has the most contact on the polished surface of the implants.

High surface roughness in L-PBF is caused by the "sintering" and partial melting of the powder particles adjacent to the components surface as well as the "stair steps effect" caused by the layer based printing process [33]. Within L-PBF melt-pool the generated spatter particles can also increase the roughness with local powder particles being able to bind to the melted material [9]. The work presented in this paper extends the range of examined laser polishing and surface modification for L-PBF produced Ti-6Al-4V samples. A CO_2 laser is studied here for reducing surface roughness and improving surface physical properties applications where antibacterial properties are required.

2. Materials, experiment and method

2.1 Additive manufacturing process
The metal AM system used in this study was a Renishaw RenAM500S which is a L-PBF machine used to produce complex geometries in a range of materials. In this case Ti-6Al-4V grade 23 ELI powder was used to produce the samples. The system has a build volume of 250mm×250mm×350mm with a heated build plate and automatic powder handling and recycling system. It uses a single 1070 nm ytterbium fibre laser which has a maximum power of 500 W and average spot size of 75 μm. The processing method used within this system is a pulsed wave/laser method, opposed to continuous laser process which is more typically used. The printing process was controlled by the laser power, point distance and exposure time, where by the laser moves between discrete points and dwells for a specified time, opposed to a continuous motion and laser power seen in continuous wave L-PBF. This system also has process monitoring capabilities using photodiodes for melt-pool monitoring and in process imagery for overall layer monitoring to ensure consistent processing. For this study samples were printed using the recommended parameters from the original equipment manufacturer using their slicing software Renishaw Quant AM V5.3. The major printing parameters are shown in Table 1 with a 60 μm layer height and 95 μm hatch distance used.

Table 1 Main printing parameters used for producing the test samples.

Feature	Laser Power (W)	Point Distance (μm)	Exposure Time (μs)
Contour	160	20	30
Hatch	200	60	70
Upskin	200	90	100

2.2 Powder used in this study
Within this study grade 23 ELI Ti-6Al-4V powder was used, supplied, and manufactured by AP&C powders with a particle size of 10 - 45 μm and D90 < 43μm. The powder was produced using plasma

atomisation and is atomisation in a high purity argon atmosphere. The powder was characterised with a highly spherical and consistent surface. Examples of powder condition taken via SEM are shown in Figure 1. The RenAM500S employs a continuous powder recycling strategy, whereby the powder is held within the system under argon, automatically sieved using an ultrasonic 63 µm sieved and transported in argon. Powder is only added to the system via the automated hopper and all powder was sieved before use, including the virgin material. The powder used within this study was tested to conform to ASTM F3001 for grade 23 specifications.
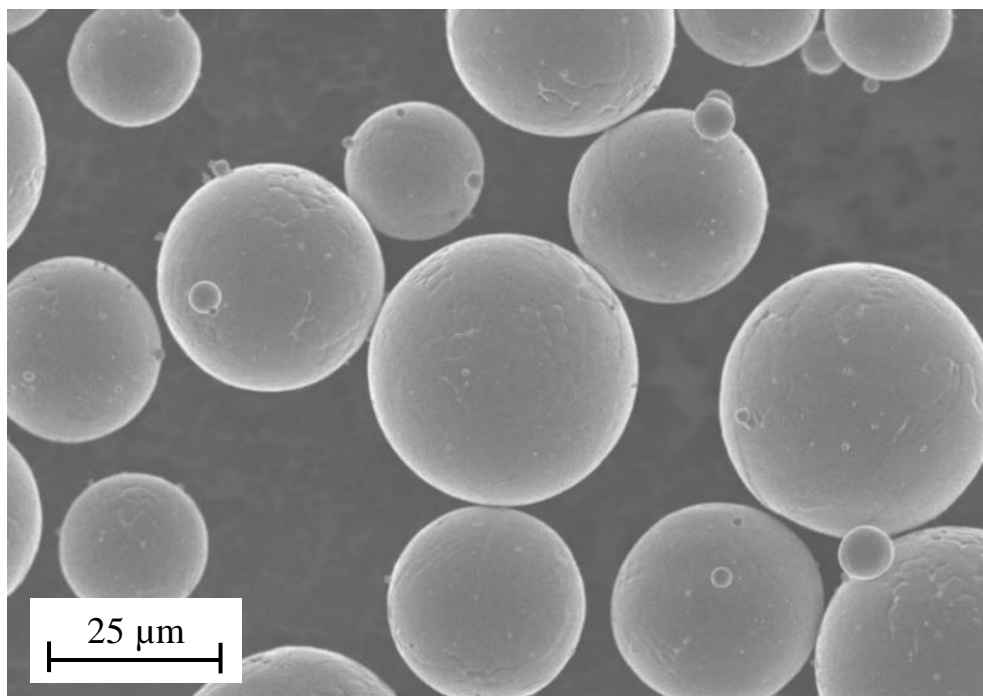

Figure 1 SEM image of Ti-6Al-4V powder showing its highly spherical nature and consistent surface finish.

2.3 Sample Geometry
For this study two sample geometries were chosen of a basic geometry, 12 mm outer diameter cylindrical (with 8 mm inner diameter) samples and a 10 mm wide flat samples. The length and wall thickness were held constant for both samples at 50 mm and 2 mm respectively. The purpose of the geometries was to test the performance on both flat and curved surfaces, however of a controlled nature for analysis. The length and thickness of the material being treated was held constant between both sample types also to minimise any thermal conduction influences on the results. The samples were produced in separate batches or a fixed size and location on the build plate of the machine, again to reduce any influences form the printing process on the sample's surfaces.

2.4 The laser polishing process

A ROFIN 1.5 kW CO_2 laser system was used during the polishing of the AM parts. The laser system and the experimental set-up are described by El Hassanin *et al*. [34]. The technical specification is listed in the following Table 2.

Table 2 The technical specification of the CO_2 laser system.

Technical specification	Value
Max. power	1500 W
Beam wavelength	10.64 μm
Beam quality factor M2	1.05
Laser focus diameter	0.2 mm
Max. scanning speed	5000 mm/min
Max. rotational speed	5000 rpm
Assist gas	Argon
Work mode	continuous

A preliminary scanning pilot test was performed in order to investigate the most significant processing parameters and their levels affecting the resulting surface roughness. The scanning strategy used in this study for both the cylindrical and flat samples is as described by Obeidi [33,35] and explained in the following Figure 2.
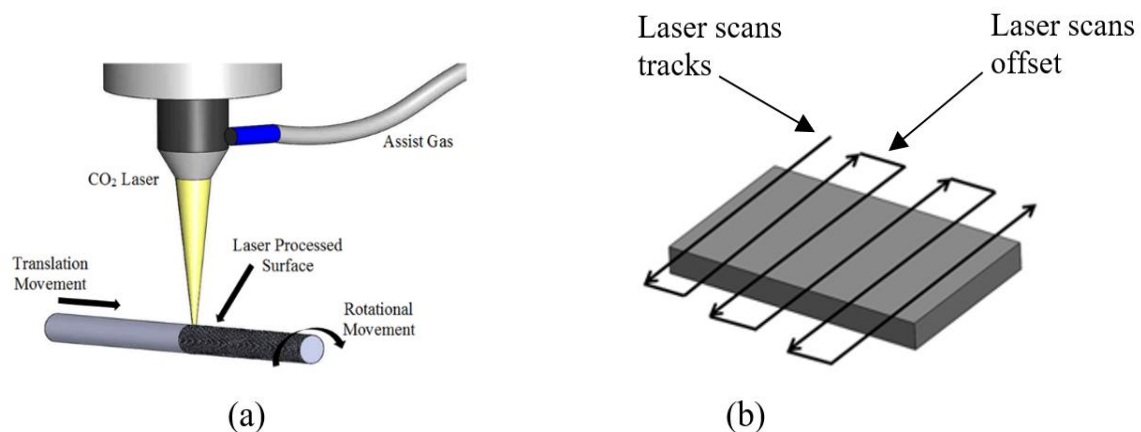

Figure 2 The scanning strategy and experimental setup for the CO_2 laser polishing of the two samples' geometries (a) cylindrical and (b) flat.

During the preliminary test, both argon and nitrogen gas were used individually to reduce the oxidation effect and protect the laser system's optics. It was noted from the early trials, that the samples processed in a nitrogen gas environment produce surfaces with a golden colouration, so nitrogen gas was avoided. On the other hand, no colour change was observed when processing with argon gas, see Figure 3, which was then used for subsequent sample preparation.
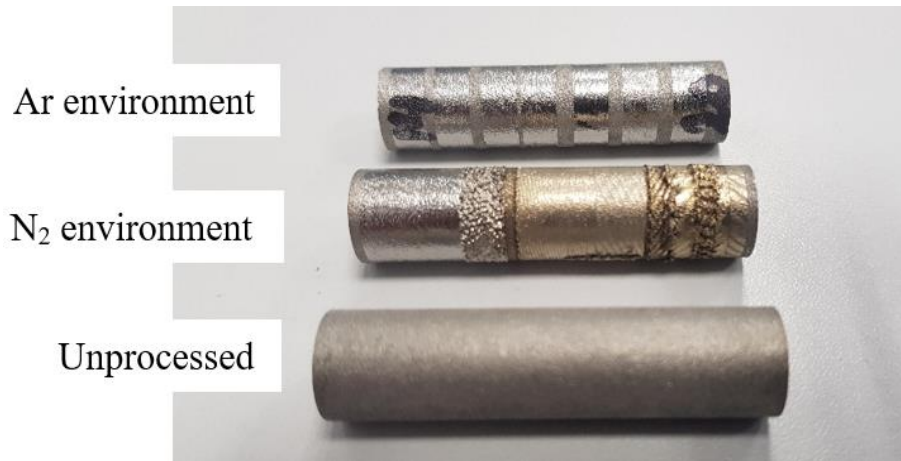
Figure 3 Ti-6Al-4V cylindrical samples investigated in this study.

In the case of the cylindrical geometry, the samples were mounted on a variable speed DC motor assembly to facilitate the rotational motion. This assembly was then mounted on the CO_2 laser's positioning stage. The stage is controlled via the CNC control system which provides the linear motion to move the laser linearly relative to the sample. The combination of the linear and rotational motions results in different overlapping laser scanning tracks (OV) covering the surface area to be scanned. Figure 2 shows a schematic of the three different percentage overlaps used in this study (25, 50, and 75%), as can be seen from Figure 4 (b, c, and d) respectively. In the higher overlapping scan tracks scenario, portions from the previously scanned surface are repeatedly scanned for up to four times (red numbering). This strategy was chosen in order to investigate the effect of the re-melting of the surface and the overlapped laser tracks on reducing the waving caused by the melting and re-solidification.
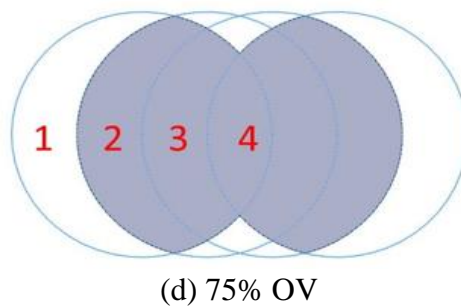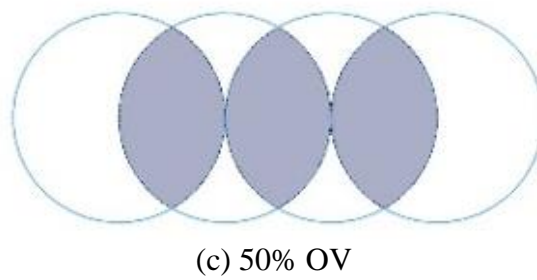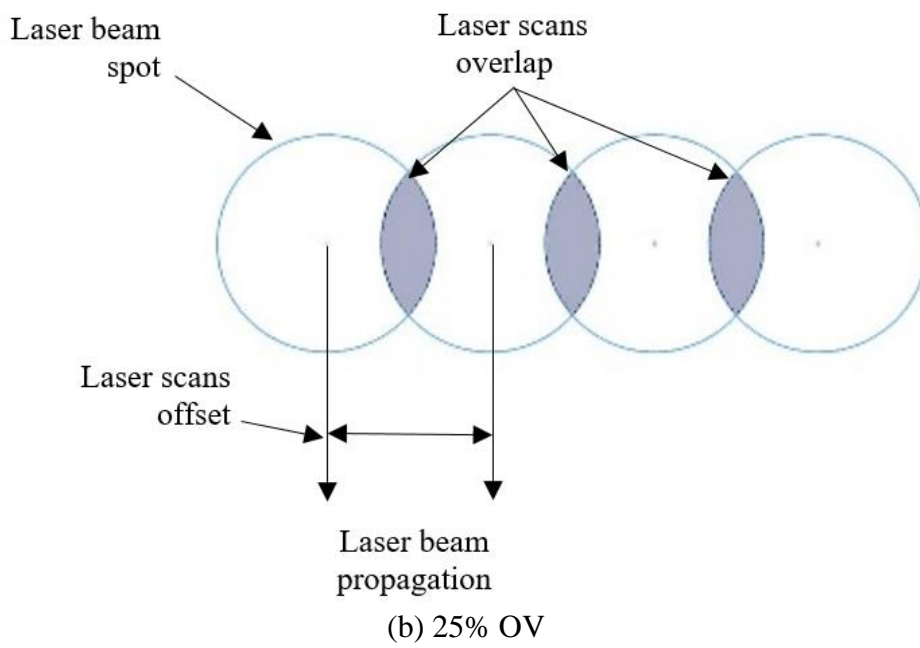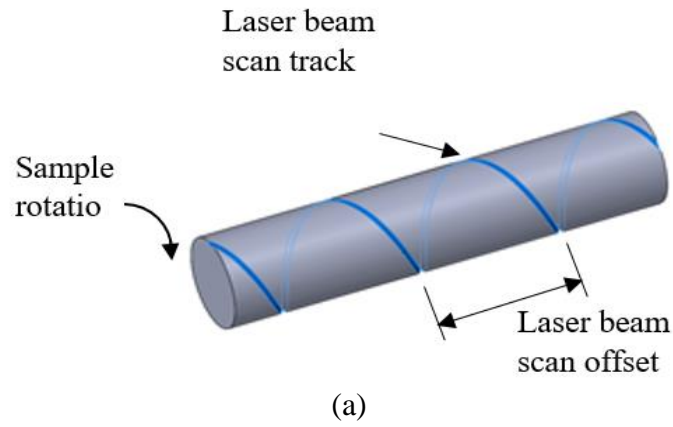
(a)

(b) 25% OV

(c) 50% OV

(d) 75% OV

Figure 4 The laser scanning strategy (a) and the three different overlap scanning scenarios (OV) used during the polishing of the cylindrical samples (b) 25, (c) 50, and (d) 75%.

A 3^3 level full factorial design of experiment (DoE) model was used for the statistical analysis of the input processing parameters and the resulting output measures. The laser spot size used was fixed to 0.2 mm located on the sample surface and the argon gas pressure was fixed to 50 kPa. The processing parameters used in this study and their levels are listed in

Table **3**.

Table **3** also lists the full range of the laser input Thermal Energy Density (TED) calculated from the following equation no. (1).

$$\text{TED (J/mm}^2) = \frac{\text{Laser beam power (W)}}{\text{Laser spot size (mm)} \times \text{Laser scanning speed} \left(\frac{mm}{sec}\right)} \; ; \qquad (1)$$

The laser scanning speed resulted from the conversion of the cylindrical sample rotation into a linear motion according to equation no. (2).

$$\text{Laser scanning speed (mm/s)} = \pi \times \text{Sample diameter (mm)} \times \text{Rotational speed (rpm)} \quad (2)$$

Table 3 The laser polishing processing parameters and their levels.

Process parameter	Level-1	Level-2	Level-3
Laser beam power, P (W)	75	125	175
Rotational speed, ω (rpm)	200	300	400
Laser scan overlap, OV (%)	25	50	75
Input energy density, E (J/mm2)	3	3.4	3.6

Another set of the cylindrical samples were processed similarly by using the same processing parameters, except by applying a laser Double-Pass (DP), i.e. processing twice with the same conditions, for comparison with the Single-Pass (SP).

For the processing of the flat samples, and for a direct comparison of the results obtained from the two sample geometries, the same input TEDs applied on the cylindrical samples were interpreted to harness the scanning strategy detailed in Figure 2 (b). New values of the input laser beam power and scanning speeds were obtained to match the input TED. Also, since the laser scanning speed applied during the polishing of the cylindrical samples is extremely high (more than 15 m/min from eq. 2) and to facilitate these parameters within the capability of the CO_2 laser system (Table 2), a fixed linear scanning speed of 4.5 m/min was applied and the new laser power values were calculated accordingly from eq. 1. These values are listed in Table 4.

2.5 The surface profile characterisation

Bruker Contour GT 3D optical microscope was used for the surface profile characterisation of both the as-build and the laser polished samples. The instrument is fitted with VISION 64 software for the

data analysis, surface profile visualisation and evaluating the surface roughness description terms. The polished samples were cleaned in a distilled water ultrasonic bath of 40 kHz for 15 minutes and dried by using hot air gun of 50 °C. For the acquisition of the surface profile data, an area of (1×1.25) mm on the cylindrical samples and (3×3) mm on the flat samples were investigated in 3 to 5 different locations for the data averaging and error bars calculations. In this study, the terms (Sa) and (Sz) will be reported and discussed and details and they can be defined as:

i. (Sa) expresses the mean of the absolute values of the surface departure above and below the mean plane within the sampling area.
ii. (Sz) expresses the average of the height difference between five highest peaks and the five lowest valleys.

2.6 X-ray diffraction Analysis

X-Ray Diffraction (XRD) characterisation was carried out using a Bruker AXS D8 diffractometer (Cu Kα radiation, λ= 0.15406 nm) to perform θ-2θ scans. The XRD spectra for an unprocessed additively manufactured Ti-6Al-4V sample, a sample processed in an argon environment, and a sample processed in a nitrogen environment were investigated for comparison of the metal phase formation.

2.7 Micrographs and metallurgy

For the sample surface inspection before and after the laser polishing and the investigation of the cross-sectional microstructure, both Zeiss EVO LS-15 scanning electron microscope SEM and Keyence-2000 optical were used. During the sample preparation for the microstructure testing, the samples were sliced by using precision cutter diamond, grinding and polished by using successive grits of silicon carbide of 200, 400, 600, 800, 1200, 2500 and 4000. A following diamond suspension of 6, 3 and 1 microns were applied for 5 to 10 minutes in a rotational speed of 250-300 rpm. Finally, and for the microstructure development, a chemical etchant made up of 15 ml of hydrofluoric acid, 10 ml nitric acid, 10 ml acetic and 5 ml of glycerol and was applied for 2 to 3 seconds.

3. Results and discussions

The as-built samples show (Sa) and (Sz) values of 17.15 and 266 μm respectively. The SEM micrographs of the unprocessed samples show partially melted and sintered particles from the surrounding powder in a micro-welding process, Figure 5 (a). This surface profile shows the high (Sz) values which consist of high and thin peaks in the 3D view obtained by the Bruker 3D optical microscope, see Figure 5 (b). Also, the SEM surface topography showed larger re-solidified melt-pools along each build layer which is the reason in the increased surface undulation. The following Figure 5 (a) shows the side view and the surface conditions of the build part where the build direction is from right to left.
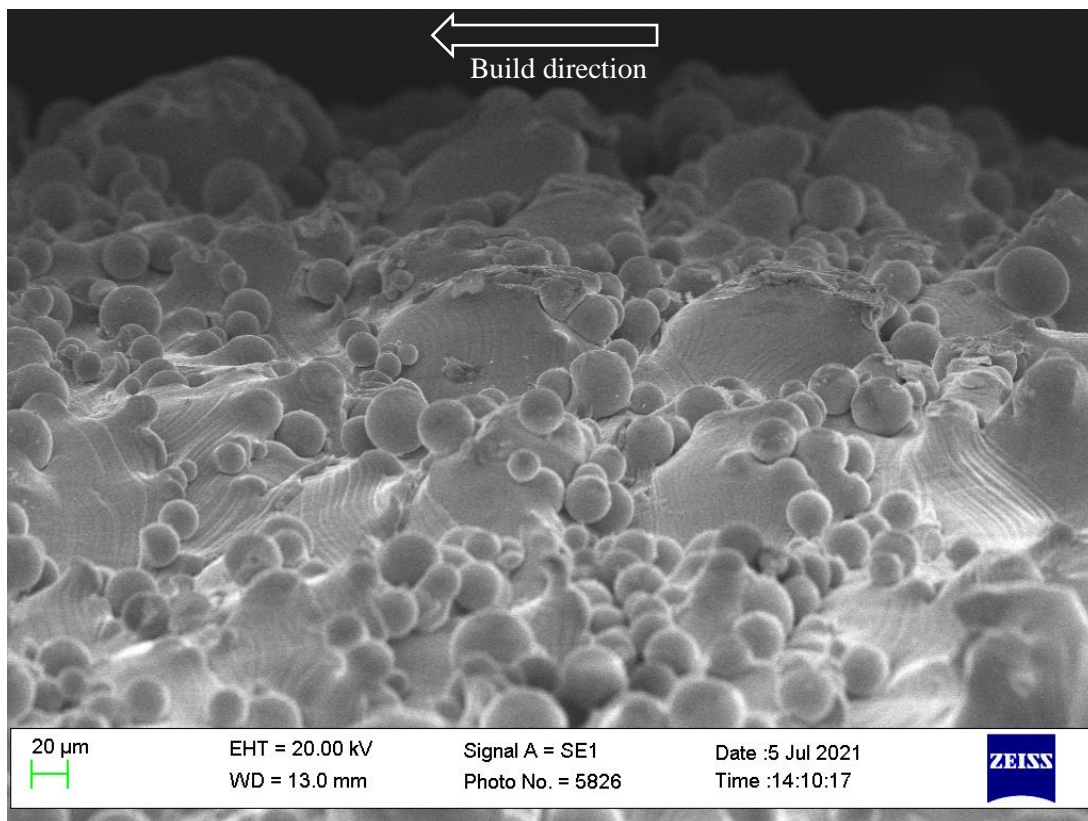
(a) SEM micrograph showing the surface topology of the as-built sample.
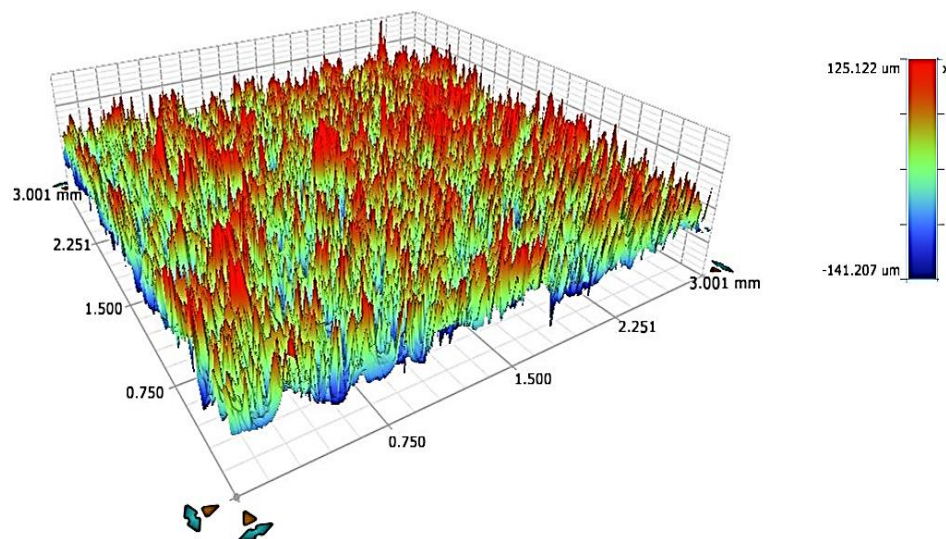
(b) 3D surface roughness profile of the as-build sample.

Figure 5 The surface profile of the as-built samples obtained by (a) SEM and (b) Bruker 3D optical microscope.

The measured surface roughness profile for the as-built samples was expected to show high values due to the sintering and partial melting of the neighbouring powder particles on the AM part as described by several studies [42–45]. This is unavoidable and for some applications i.e. aerospace

and biomedical, it can be regarded as a limitation of AM process which is why post-processing by polishing is essential.

The following Table 4 lists the (Sa) and (Sz) values with the input processing parameters for the full set of the cylindrical samples corresponding to the 3^3 full factorial DoE model.

Table 4 The input laser polishing processing parameters and the corresponding measured average surface profile values (Sa) and (Sz) for the cylindrical samples, n=3.

| Sample No.	Laser power (W)	Rotational speed (rpm)	Scan overlap (%)	Energy density (J/mm²)	SP-Sa (μm)	DP-Sa (μm)	SP-Sz (μm)	DP-Sz (μm)
1	75	400	50	2.24	4.77±0.52	6.73±0.56	46.83±10.51	43.81±6.16
2	75	300	25	2.49	7.27±0.61	5.47±0.84	73.19±5.20	133.17±24.82
3	175	400	25	4.48	6.10±0.55	6.74±0.90	61.59±9.58	39.68±6.50
4	175	300	75	8.36	3.64±0.50	4.98±0.52	25.70±7.25	35.47±5.92
5	125	300	50	5.07	5.83±0.59	7.52±0.70	51.20±18.83	34.33±7.09
6	175	200	50	10.74	10.30±1.10	4.45±0.61	144.22±26.58	35.84±7.06
7	125	400	50	3.80	5.60±0.75	5.90±0.80	67.31±16.51	31.34±5.62
8	75	300	75	3.48	7.42±0.72	5.40±0.58	55.81±7.81	32.95±9.42
9	175	400	75	6.27	3.97±0.52	4.43±0.69	31.94±5.29	36.21±6.55
10	125	200	50	7.61	7.63±0.72	4.46±0.94	82.65±11.81	51.94±7.20
11	175	400	50	5.37	4.77±0.87	4.81±0.71	36.65±5.01	48.26±12.51
12	125	400	75	4.44	4.27±0.61	3.94±0.51	41.74±7.21	38.82±6.84
13	75	300	50	2.98	7.13±0.54	4.83±0.66	65.07±19.16	63.02±22.18
14	75	200	50	4.48	5.98±0.89	5.93±0.75	53.46±8.86	52.28±14.13
15	175	300	50	7.16	5.44±0.67	6.65±0.78	44.20±7.19	40.24±5.50
16	125	200	75	8.88	10.99±0.85	5.16±0.55	153.21±20.52	56.35±8.18
17	175	200	75	12.53	9.20±0.88	5.64±0.63	67.93±11.85	48.64±6.50
18	175	300	25	5.97	4.49±0.77	6.69±0.58	39.13±6.58	43.87±8.20
19	125	300	25	4.23	8.38±1.00	7.21±0.82	91.12±14.84	59.17±14.49
20	75	200	75	5.22	4.92±0.68	6.27±1.00	37.05±7.82	55.82±6.97
21	125	300	75	5.92	4.83±0.50	5.55±0.71	43.22±9.18	43.34±6.07
22	75	200	25	3.73	6.94±0.94	5.28±0.58	44.69±14.97	68.08±8.050
23	75	400	75	2.61	6.52±0.81	4.84±0.50	50.14±9.84	69.74±8.15
24	125	400	25	3.17	6.66±0.65	7.59±0.67	70.89±6.20	40.50±5.92
25	125	200	25	6.34	6.47±0.72	4.45±0.51	103.73±23.02	57.80±8.20
26	75	400	25	1.87	6.09±0.81	6.54±0.52	75.85±18.25	41.94±6.50
27	175	200	25	8.95	6.96±0.57	4.03±0.70	99.31±15.06	41.93±7.10

Note: The iteration of measurement was performed in different locations for at least (n=3). The ± value indicates 95% confidence interval for the mean surface profile.

From Table 4, sample no. 4 (green shade) showed the lower (Sa) value of 3.636 μm processed with the higher level of laser beam power of 175 W, medium rotational speed of 300 rpm and the higher-level overlap of 75%. The Response Surface Method (RSM) graph for this sample is shown in Figure 7 (b) (left). These laser parameters resulted in a laser input TED of 8.36 J/mm². The enhancement in the surface roughness and (Sa) values is more prone to occur with the high percentage overlap of the scanning tracks as can be seen in Figure 6 (b and c) processed by using the medium and high rotational speed. The increase in the (OV) also contributes in trimming of the waving material between the build

layers and successive laser tracks created by both the laser melting in both SLM and laser polishing processes respectively. This melting and relocation of the material reduces the (Sa) and (Sz) values which represents the total distance between the higher peak and the lower valley's bottom. The modified surface in Figure 6 (b) shows a more solid and continuous profile than the discrete peaks of the unprocessed surface. In contrast, the lower (ω) values, results in increased OV values and thus applies excessive melting and increased (Sz), see Figure 6 (c) corresponds to sample no.6.
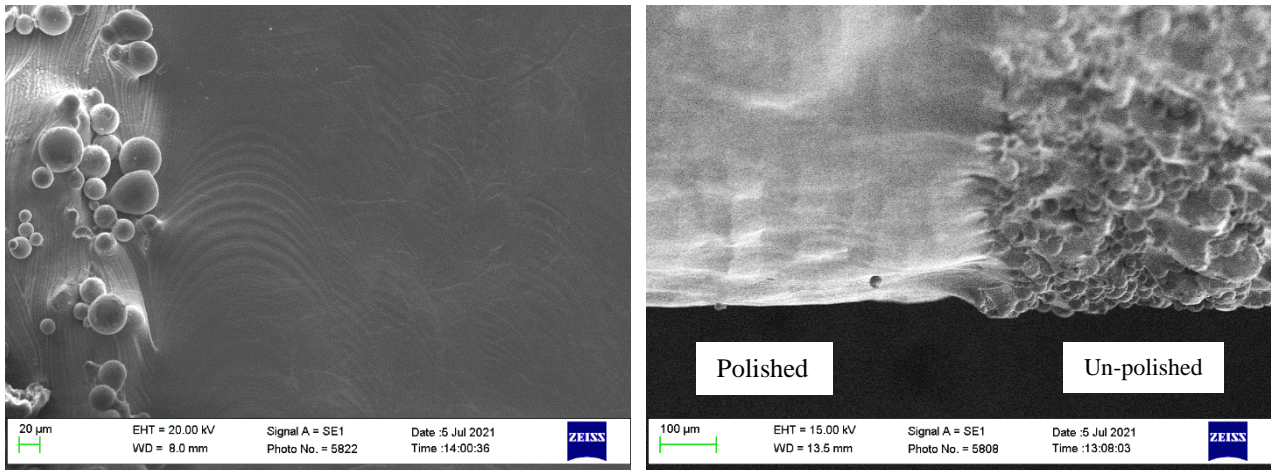

(a)
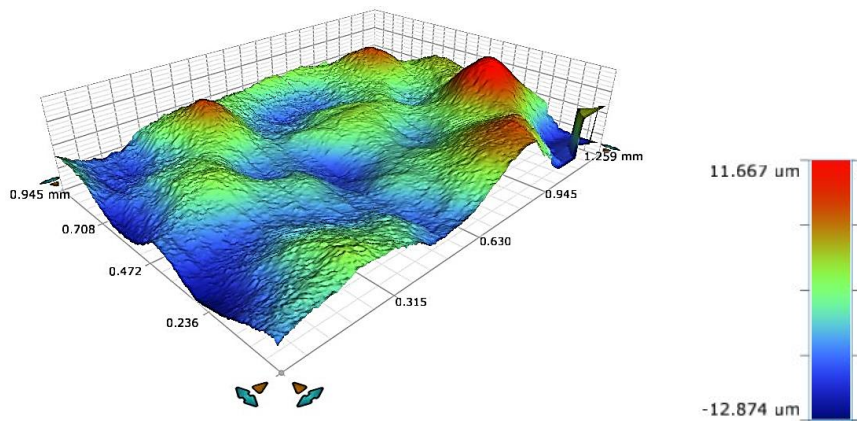
(b)
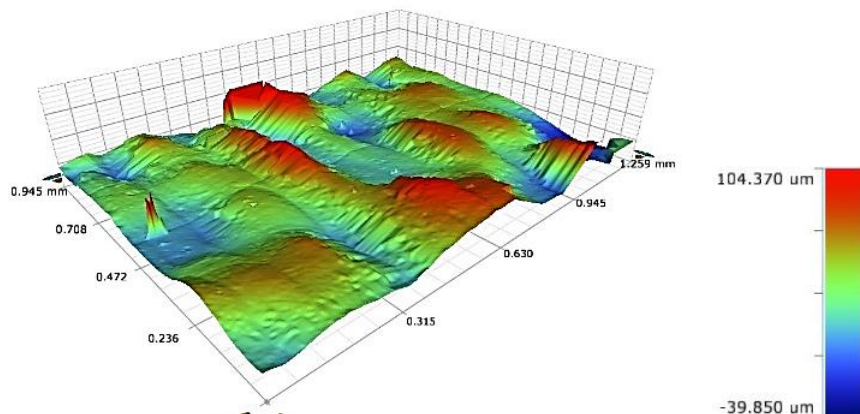
(c)

Figure 6 (a), and (b) SEM and OM micrographs of sample no. 4, and

(c) OM image of sample no.6 listed in Table 4.

In Figure 7 (a), it was noted that (Sa) values were significantly improved when the lower (OV) values were applied. When the high-power level of 175 W was applied in a combination with the lower rotational speed of 200 rpm and (OV) greater than 50%, limited or reduced improvement was observed as can be seen in samples no. 6, 16 and 17 (red shaded cells in Table 4). This degradation is caused by the over and re-remelting of the surface which is already polished by the previous scan tracks thus, roughening and increase of (Sa) values were obtained. Nevertheless, (Sz) values showed acceptable improvement as an indicating the dislocation of the materials from the high peaks to the lower valleys.

## 3.1 The re-melting by laser beam double pass (DP)

Once the optimised combination of the process parameters was achieved, laser SP can be sufficient to produce the minimum achievable surface conditions. The re-melting with the (DP) can negatively affect the surface roughness, see Figure 7 (b and c) (right). Nevertheless, the double-pass processing improved most of the poor results obtained from the single-pass (SP) processed with the lower rotational speed 200 rpm, Figure 7 (a). In the latter scenario, a limited improvement in (Sa) was noted in the lower power value 75 W compared to (SP). The best improvement obtained from the processing with (DP) was in the case of samples no. 6 and 17 and reducing (Sa) from 10.3 to 4.4 microns and 9.2 to 5.6 microns respectively.
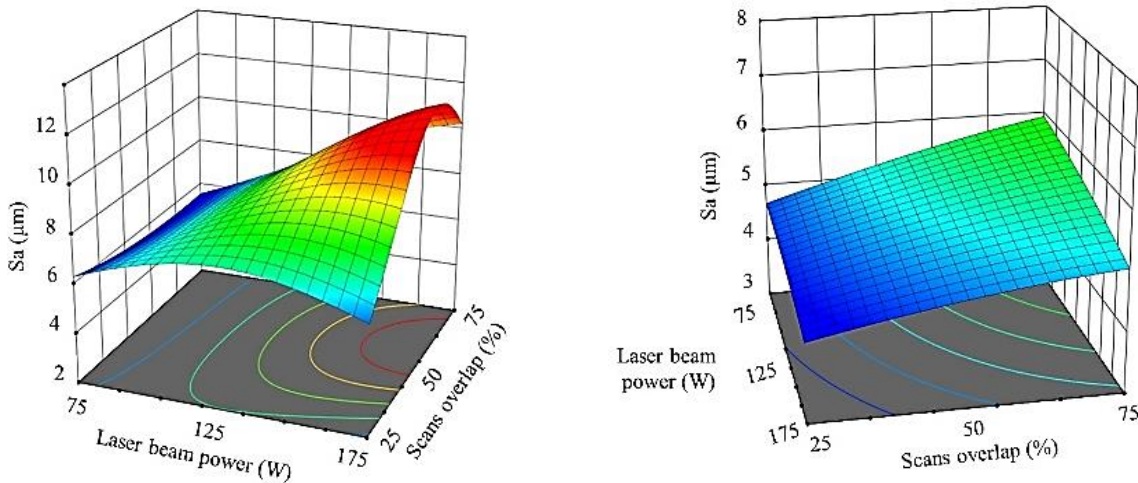
(a) 200 rpm SP (left) DP (right)
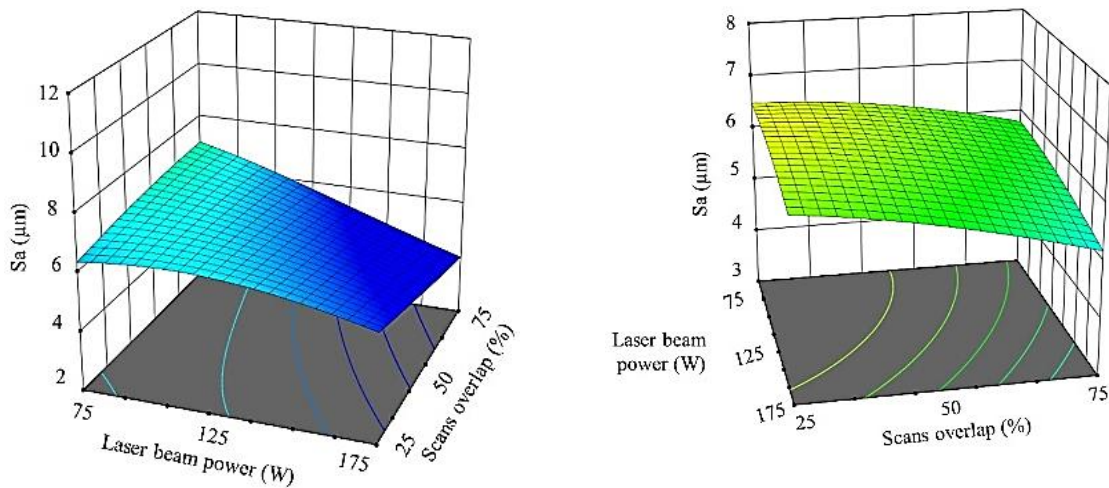
(a) 300 rpm SP (left) DP (right)
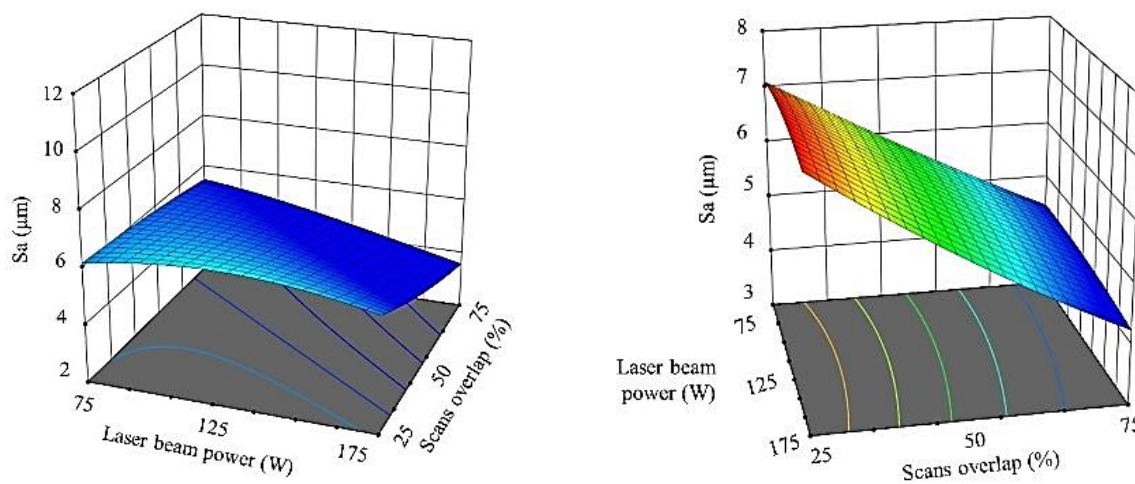
(a) 400 rpm SP (left) DP (right)

Figure 7 The response surface method (RSM) graphs showing the effect of the input processing parameters on the output measured surface roughness (Sa) for the single (SP)and double laser pass (DP).

Pearson standard analysis was applied on the results obtained to establish any correlation with the input parameters and the nature of this correlation. A correlation factor, r, of 0.3 or above and a significance level, p, of 0.05 or below is an indication of an existing strong correlation, with lower p values indicating a degree of higher significance in the correlation.

Table 5 indicates negative correlations between (Sa) versus the laser beam power and the rotational speed (green shaded cells) for the applied range of these factors. The decrease in the rotational speed results in re-melting and roughening of the processed surface. The increase in the laser beam power leads to the sufficient melting of the high peaks to be relocated in the lower valleys and depressed areas. Nevertheless, a combination of both high laser power and low scanning speed might be deleterious and increased (Sa) values can be achieved.

Table 5 The correlation strength between the input processing Parameters and the output measured (Sa) value obtained by Pearson correlation standard.

Processing Mode	Pearson Value	P (W)	ω (rpm)	OV (%)	TED (J/mm3)
SP	r =	**-0.4941**	**-0.5205**	-0.0909	-0.0859
	p =	**0.0088**	**0.0054**	0.6520	0.6699
DP	r =	-0.1229	0.2530	-0.3371	-0.3482
	p =	0.5414	0.2028	0.0855	0.0751

No similar, clear, or strong correlation was noted when processing the surface by laser beam re-melting (double-pass DP). If the optimum enhancement can be reached by a laser single-pass, the laser processing efficiency is increased, saving time and consumable costs. Considering the time consumed to produce sample no. 4, the cost to laser polish the sample can be estimated by using the equation (3) below.

$$Cost = \ processing\ time\ \left(10\frac{s}{cm^2}\right) * laser\ \&\ operator\ charges\left(100\frac{€}{h}\right) = \ \left(0.27\frac{€}{cm^2}\right) \quad (3)$$

3.2 Flat sample polishing

Table 6 below, lists the resulted (Sa) and (Sz) values of the flat samples processed as explained in (section 2.4). Similar (Sa) and (Sz) values were observed during the polishing of the flat samples. No strong correlations between the (Sa) values and the input processing parameters nor with (Sa) values of the cylindrical samples were noted. This result indicates the significant possibility to polish the samples in different geometries by using the same range of the input processing parameters and thermal energy density.

Table 6 Lists the input processing parameters and the measured output (Sa) and (Sz) values obtained from polishing the cylindrical and flat Ti-6Al-4V samples (The scanning speed fixed at 4.5 m/min, section 2.4).

Sample No.	Laser power (W)	TED (J/mm2)	Cylindrical samples	Flat samples	
			Sa (µm)	Sa (µm)	Sz (µm)
1	45	2.24	4.774	5.201	99.31
2	45	2.49	7.274	4.681	139.35
3	45	4.48	6.096	4.92	67.93
4	76	8.36	3.636	5.543	103.74
5	76	5.07	5.828	5.545	82.65
6	76	10.74	5.89	8.474	153.21
7	107	3.80	5.603	5.248	44.7
8	107	3.48	7.424	5.064	53.46
9	107	6.27	3.97	5.548	37.05
10	30	7.61	7.632	6.751	73.19
11	30	5.37	4.771	5.818	65.08
12	30	4.44	4.274	5.885	55.82
13	51	2.98	7.129	5.071	91.13
14	51	4.48	10.298	5.398	51.2
15	51	7.16	5.443	6.844	43.23
16	70	8.88	10.988	8.062	39.13
17	70	12.53	4.921	3.306	44.2
18	70	5.97	4.493	5.219	25.7
19	22	4.23	8.38	5.584	75.85
20	22	5.22	9.201	3.88	46.83
21	22	5.92	4.833	5.433	50.15
22	37	3.73	6.956	6.055	70.9
23	37	2.61	6.519	5.076	67.32
24	37	3.17	6.658	4.784	41.74
25	54	6.34	6.468	5.875	61.59
26	54	1.87	6.087	6.193	36.65
27	54	8.95	6.941	6.926	31.95

A reduction of 0.02 mm was noted in the processed sample diameter for the before (12.02±0.01) mm and after (12.00±0.01) mm laser polishing measured on the samples with the lower (Sa) values, *i.e.*, samples no. 4 and 9. In the cross-sectional view, the modified layer for these samples showed variant melt-depth between 10 to 120 microns, Figure 8 (b). Also, no voids, defects or any pores presence was observed in this layer due to the re-melting. A such layer and surface finishing could improve the fatigue life. On the other hand, laser polishing can also deteriorate the fatigue strength if surface flaws (i.e. porosities and cracks) or residual stresses are introduced. Avilés et al. [32] reported a fatigue resistance at 10^6 cycles of 461MPa for the as-printed and 420MPa for laser polished AISI 1045 steel. A study on L-PBF Ti-6Al-4V reported 120 MPa fatigue strength on both treated and untreated samples [39]. Similar to the observed in Figure 9, they also reported an increase in hardness in the laser polished samples. It is well-known that there is a positive correlation between fatigue limit and hardness [46]. Therefore, it is possible that some of the here laser polished samples held improved fatigue strength.

(a)
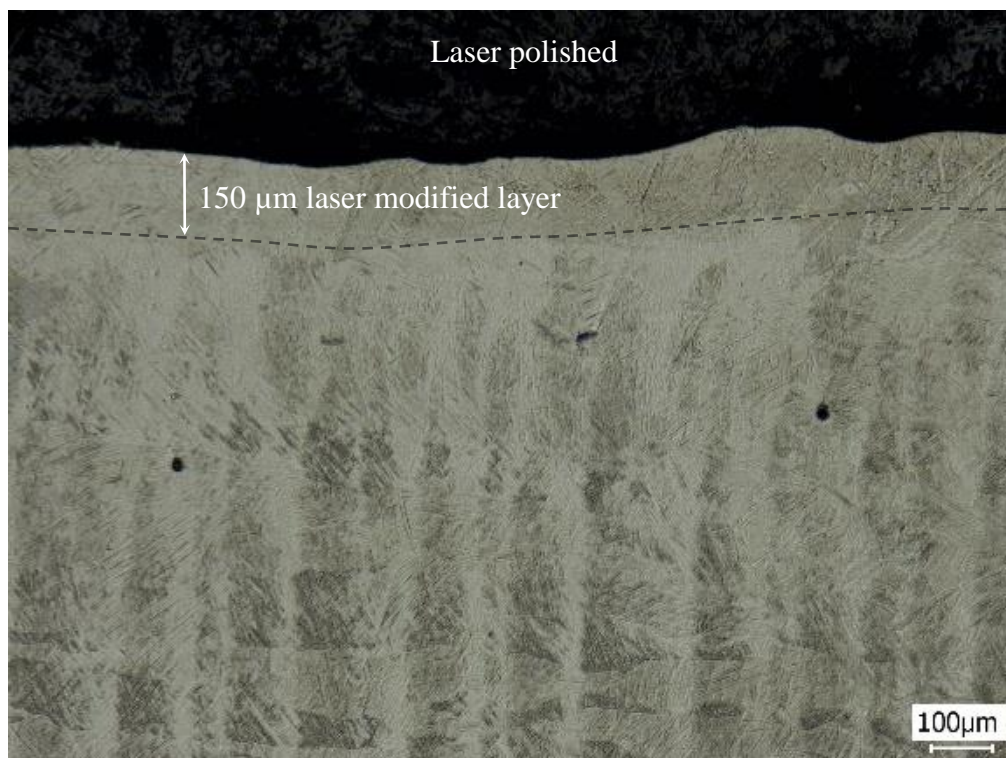
(b)

Figure 8 SEM images of the surface before (left) and after (right) laser polishing.

An increase in the modified layer hardness from the average of 485 to 520 HV was observed in a depth of 100 to 150 μm from the sample surface, Figure 9. A similar result was reported by El

Hassanin et al. [45], which was said to be due to the precipitation of the silicon in the molten and re-solidified polished layer. In this study and from the x-ray results shown in Figure 10, no alteration in the modified layer phase composition was noted compared to the unprocessed samples. This increase in the surface hardness can be explained by the instant melting and re-solidification of a thin layer of the metal at the presence of the assist gas stream in a process similar to laser hardening and glazing.
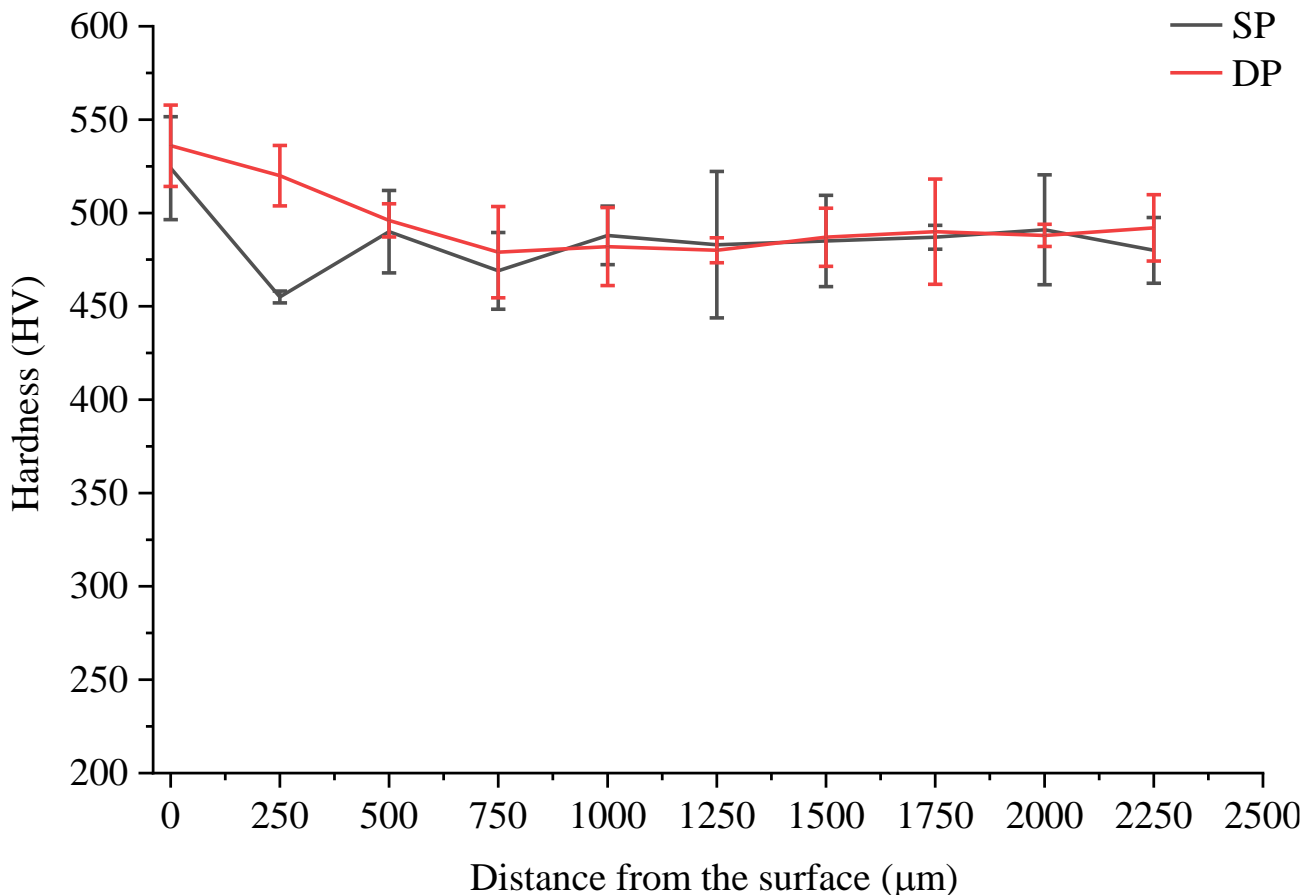

Figure 9 The micro-hardness measured from the polished surface to the bulk material

in the cross-sectional direction.

3.3 X-ray results

The unprocessed and argon environment samples show similar spectra, which are consistent with α phase, hexagonally close-packed titanium. The sample processed in a nitrogen environment, which exhibited a visibly altered, darker golden surface colour, shows a changed spectrum. The α phase peaks are significantly reduced. The new peak at 39 ° indicates the presence of β phase, body-centred cubic titanium, which was not detectable in the other samples. α phase titanium alloys have greater oxidisation and corrosion resistance, while β phase are more deformable and readily heat treatable [47,48]. The strongest peak at 43 ° indicates titanium nitride compounds which was also reported in the literature [49] and a compositional change in the sample surface. Zeng et al. [50] reported on laser nitriding of titanium surfaces, where a similar peak at this position was produced in samples processed with low scanning speed. The authors reported these samples having a visibly darker golden colour, complete dendritic nitride layer, improved corrosion resistance, and increased surface hardness.

These results indicate that the sample processed in the argon environment has not undergone significant compositional or microstructural changes compared with the unprocessed material, while the sample processed in the nitrogen environment has undergone significant changes.

The XRD spectra for an un-processed additively manufactured Ti-6Al-4V sample, a sample processed in an argon environment, and a sample processed in a nitrogen environment are shown in Figure 10 (a). A closer scan from 30-45 ° for the un-processed and nitrogen environment sample is shown in Figure 10 (b).
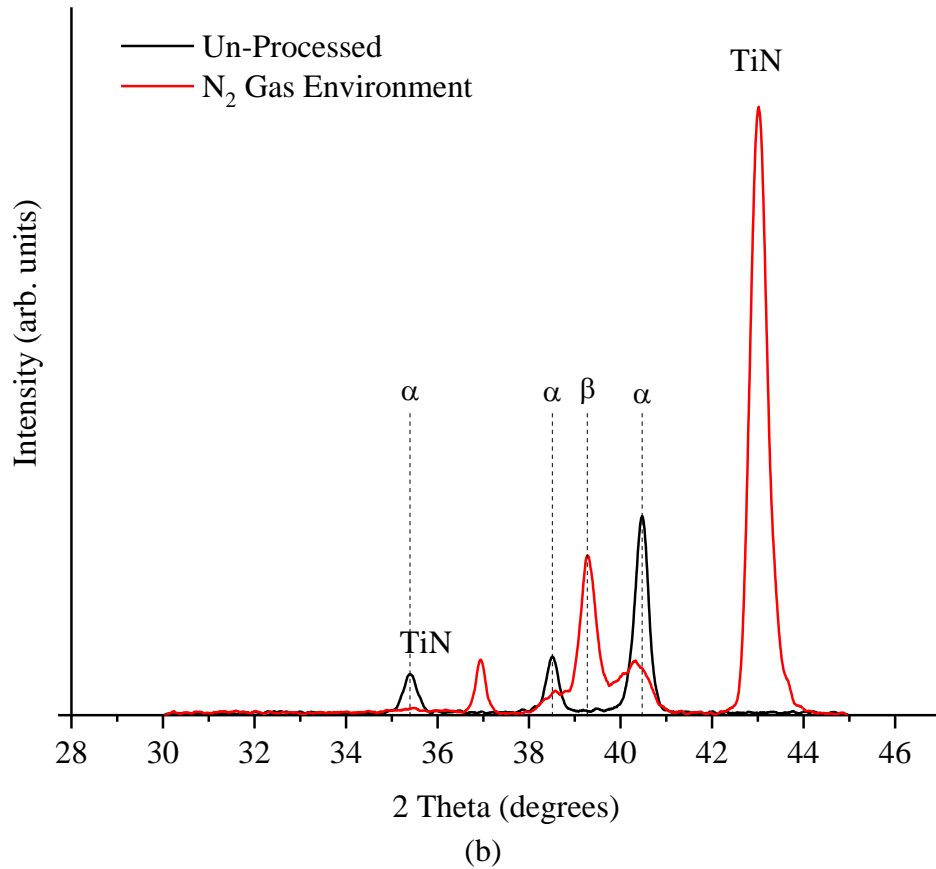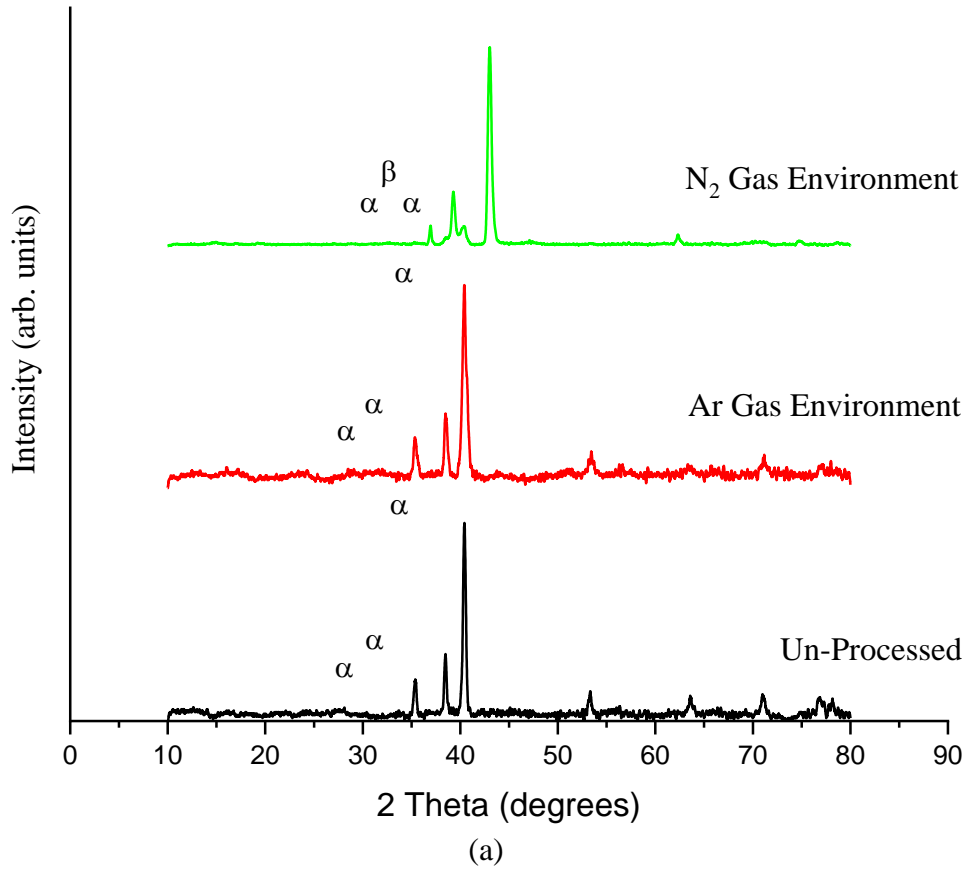
(a)

(b)

Figure 10 (a) X-ray Diffraction (XRD) patterns of the Ti-6Al-4V parts produced by Laser Powder Bed Fusion (L-PBF) before and after laser surface processing, (b) a magnified view of the unprocessed and N2 environment processed sample.

4. Conclusions

In this work, CO_2 laser irradiation was used in continuous mode for the surface modification and polishing of additively manufactured Ti-6Al-4V. The study confirmed the possibility to achieve sufficient improvement in the surface conditions of the samples produced in cylindrical and flat geometries. It was found that both the laser beam power and the scanning speed have strong, inverse correlation with the resulting surface roughness within the applied range of the processing parameters. The percentage overlap of the laser scanning tracks has a robust effect on the measured outputs depending on the laser beam power and scanning speed applied, the combination of lower speed and high-power levels can negatively affect the surface roughness due to excessive melting. This effect was clearly eliminated in other scenarios when lower power levels and/or higher scanning speeds were employed.

Processing by the double-pass (DP) and re-melting, decreases the high (S_a) values obtained from the single-pass (SP). For example, sample no. 16 in Table 4 showed the maximum value of 10.988 μm and was reduced to 5.162 μm after the second laser pass. Also, the maximum (S_a) value recorded using this method was found to be 7.586 μm for sample no. 24. Similar lower values were recorded for the two methods as an indication that no further optimisation can be achieved.

The thermal energy density (TED) is a good approximation term to be used in the interpretation of the processing parameters and reflect them on the processing of similar material but different geometry. Nevertheless, it is not necessary to produce the exact same surface profile (S_a) and (S_z) values when equivalent values were applied in equation (1) to give the same (TED). The data listed in Table 6 comparing the modified surface conditions obtained from the cylindrical and flat geometries showed similar range of values. The differences and change in the order of these values are caused by applying different values of laser power and scanning speed despite the same values of (TED). Moreover, the different geometry contributes in changing the dislocation of the molten material due to the centrifugal force and erosion caused by assist gas ejection over the cylindrical and flat surfaces.

As aforementioned, in this study L-PBF Ti-6Al-4V cylindrical and flat geometries were successfully laser polished. More complex L-PBF components are also laser polish treatable. For example, a high precision multi-axes, variable speed and computer-controlled positioning stage can be employed, in which, the surface profile can be programmed into the control system to generate multi-axes interpolation under the fixed laser head. This could be an alternative for components which surface finishing is critical, or machining is difficult.

References

[1] Huang, R., Riddle, M., Graziano, D., Warren, J., Das, S., Nimbalkar, S., Cresko, J., and Masanet, E., 2016, "Energy and Emissions Saving Potential of Additive Manufacturing: The Case of Lightweight Aircraft Components," J. Clean. Prod., **135**, pp. 1559–1570.

[2] Lütjering, G., and Williams, J. C., 2007, *Titanium*, Springer Science & Business Media, New York.

[3] Heinl, P., Müller, L., Körner, C., Singer, R. F., and Müller, F. A., 2008, "Cellular Ti–6Al–4V Structures with Interconnected Macro Porosity for Bone Implants Fabricated by Selective Electron Beam Melting," Acta Biomater., **4**(5), pp. 1536–1544.

[4] Mandolfino, C., Obeidi, M., Lertora, E., and Brabazon, D., 2020, "Comparing the Adhesion Strength of 316L Stainless Steel Joints after Laser Surface Texturing by CO2 and Fiber Lasers," Int. J. Adv. Manuf. Technol., **109**(3), pp. 1059–1069.

[5] Ahmed Obeidi, M., Uí Mhurchadha, S. M., Raghavendra, R., Conway, A., Souto, C., Tormey, D., Ahad, I. U., and Brabazon, D., 2021, "Comparison of the Porosity and Mechanical Performance of 316L Stainless Steel Manufactured on Different Laser Powder Bed Fusion Metal Additive Manufacturing Machines," J. Mater. Res. Technol., **13**, pp. 2361–2374.

[6] Mussatto, A., Groarke, R., O'Neill, A., Obeidi, M. A., Delaure, Y., and Brabazon, D., 2021, "Influences of Powder Morphology and Spreading Parameters on the Powder Bed Topography Uniformity in Powder Bed Fusion Metal Additive Manufacturing," Addit. Manuf., **38**.

[7] Obeidi, M. A., McCarthy, E., Kailas, L., and Brabazon, D., 2018, "Laser Surface Texturing of Stainless Steel 316L Cylindrical Pins for Interference Fit Applications," J. Mater. Process. Technol., **252**, pp. 58–68.

[8] Fitzsimons, L., McNamara, G., Obeidi, M. A., and Brabazon, D., 2020, "The Circular Economy: Additive Manufacturing and Impacts for Materials Processing," *Encyclopedia of Renewable and Sustainable Materials*, Elsevier.

[9] Ahmed Obeidi, M., Mussatto, A., Groarke, R., Vijayaraghavan, R. K., Conway, A., Rossi Kaschel, F., McCarthy, E., Clarkin, O., O'Connor, R., and Brabazon, D., 2020, "Comprehensive Assessment of Spatter Material Generated during Selective Laser Melting of Stainless Steel," Mater. Today Commun., **25**.

[10] Mussatto, A., Ahad, I. U., Mousavian, R. T., Delaure, Y., and Brabazon, D., 2021, "Advanced Production Routes for Metal Matrix Composites," Eng. Rep., **3**(5).

[11] Hassanin, A. E., Troiano, M., Scherillo, F., Silvestri, A. T., Contaldi, V., Solimene, R., Scala, F., Squillace, A., and Salatino, P., 2020, "Rotation-Assisted Abrasive Fluidised Bed Machining of AlSi10Mg Parts Made through Selective Laser Melting Technology," Procedia Manuf., **47**, pp. 1043–1049.

[12] Ataee, A., Li, Y., Fraser, D., Song, G., and Wen, C., 2018, "Anisotropic Ti-6Al-4V Gyroid Scaffolds Manufactured by Electron Beam Melting (EBM) for Bone Implant Applications," Mater. Des., **137**, pp. 345–354.

[13] Sallica-Leva, E., Caram, R., Jardini, A. L., and Fogagnolo, J. B., 2016, "Ductility Improvement Due to Martensite A′ Decomposition in Porous Ti–6Al–4V Parts Produced by Selective Laser Melting for Orthopedic Implants," J. Mech. Behav. Biomed. Mater., **54**, pp. 149–158.

[14] Dinda, G. P., Song, L., and Mazumder, J., 2008, "Fabrication of Ti-6Al-4V Scaffolds by Direct Metal Deposition," Metall. Mater. Trans. A, **39**(12), pp. 2914–2922.

[15] Hollander, D. A., von Walter, M., Wirtz, T., Sellei, R., Schmidt-Rohlfing, B., Paar, O., and Erli, H.-J., 2006, "Structural, Mechanical and in Vitro Characterization of Individually Structured Ti–6Al–4V Produced by Direct Laser Forming," Biomaterials, **27**(7), pp. 955–963.

[16] Murr, L. E., Gaytan, S. M., Medina, F., Lopez, H., Martinez, E., Machado, B. I., Hernandez, D. H., Martinez, L., Lopez, M. I., Wicker, R. B., and Bracke, J., 2010, "Next-Generation Biomedical Implants Using Additive Manufacturing of Complex, Cellular and Functional Mesh Arrays," Philos. Transact. A Math. Phys. Eng. Sci., **368**(1917), pp. 1999–2032.

[17] Liu, S., and Shin, Y. C., 2019, "Additive Manufacturing of Ti6Al4V Alloy: A Review," Mater. Des., **164**.

[18] Ribeiro, M. V., Moreira, M. R. V., and Ferreira, J. R., 2003, "Optimization of Titanium Alloy (6Al–4V) Machining," J. Mater. Process. Technol., **143–144**, pp. 458–463.

[19] Rahman, M., Wang, Z.-G., and Wong, Y.-S., 2006, "A Review on High-Speed Machining of Titanium Alloys," JSME Int. J. Ser. C Mech. Syst. Mach. Elem. Manuf., **49**(1), pp. 11–20.

[20] Bartolomeu, F., Buciumeanu, M., Pinto, E., Alves, N., Silva, F. S., Carvalho, O., and Miranda, G., 2017, "Wear Behavior of Ti6Al4V Biomedical Alloys Processed by Selective Laser Melting, Hot Pressing and Conventional Casting," Trans. Nonferrous Met. Soc. China, **27**(4), pp. 829–838.

[21] Bian, L., Thompson, S. M., and Shamsaei, N., 2015, "Mechanical Properties and Microstructural Features of Direct Laser-Deposited Ti-6Al-4V," JOM, **67**(3), pp. 629–638.

[22] Doğu, M. N., Esen, Z., Davut, K., Tan, E., Gümüş, B., and Dericioglu, A. F., 2020, "Microstructural and Texture Evolution during Thermo-Hydrogen Processing of Ti6Al4V Alloys Produced by Electron Beam Melting," Mater. Charact., **168**.

[23] Donachie, M. J., 2000, *Titanium: A Technical Guide*, ASM International.

[24] Cui, C., Hu, B., Zhao, L., and Liu, S., 2011, "Titanium Alloy Production Technology, Market Prospects and Industry Development," Mater. Des., **32**(3), pp. 1684–1691.

[25] Singh, P., Pungotra, H., and Kalsi, N. S., 2017, "On the Characteristics of Titanium Alloys for the Aircraft Applications," Mater. Today Proc., **4**(8), pp. 8971–8982.

[26] Uhlmann, E., Kersting, R., Klein, T. B., Cruz, M. F., and Borille, A. V., 2015, "Additive Manufacturing of Titanium Alloy for Aircraft Components," Procedia CIRP, **35**, pp. 55–60.

[27] Gurrappa, I., 2003, "Characterization of Titanium Alloy Ti-6Al-4V for Chemical, Marine and Industrial Applications," Mater. Charact., **51**(2), pp. 131–139.

[28] Weißmann, V., Bader, R., Hansmann, H., and Laufer, N., 2016, "Influence of the Structural Orientation on the Mechanical Properties of Selective Laser Melted Ti6Al4V Open-Porous Scaffolds," Mater. Des., **95**, pp. 188–197.

[29] Strano, G., Hao, L., Everson, R. M., and Evans, K. E., 2013, "Surface Roughness Analysis, Modelling and Prediction in Selective Laser Melting," J. Mater. Process. Technol., **213**(4), pp. 589–597.

[30] Desrousseaux, C., Sautou, V., Descamps, S., and Traoré, O., 2013, "Modification of the Surfaces of Medical Devices to Prevent Microbial Adhesion and Biofilm Formation," J. Hosp. Infect., **85**(2), pp. 87–93.

[31] Larsson, C., Thomsen, P., Lausmaa, J., Rodahl, M., Kasemo, B., and Ericson, L. E., 1994, "Bone Response to Surface Modified Titanium Implants: Studies on Electropolished Implants with Different Oxide Thicknesses and Morphology," Biomaterials, **15**(13), pp. 1062–1074.

[32] Avilés, R., Albizuri, J., Lamikiz, A., Ukar, E., and Avilés, A., 2011, "Influence of Laser Polishing on the High Cycle Fatigue Strength of Medium Carbon AISI 1045 Steel," Int. J. Fatigue, **33**(11), pp. 1477–1489.

[33] Obeidi, M. A., McCarthy, E., O'Connell, B., Ul Ahad, I., and Brabazon, D., 2019, "Laser Polishing of Additive Manufactured 316L Stainless Steel Synthesized by Selective Laser Melting," Mater. Basel Switz., **12**(6), p. E991.

[34] El Hassanin, A., Obeidi, M. A., Scherillo, F., and Brabazon, D., 2021, "CO2 Laser Polishing of Laser-Powder Bed Fusion Produced AlSi10Mg Parts," Surf. Coat. Technol., **419**.

[35] Obeidi, M. A., 2018, "Laser Processing of Metallic Surfaces for Controlled Micro-Texturing and Metallic Bonding," PhD, Dublin City University.

[36] Qian, G., Jian, Z., Pan, X., and Berto, F., 2020, "In-Situ Investigation on Fatigue Behaviors of Ti-6Al-4V Manufactured by Selective Laser Melting," Int. J. Fatigue, **133**.

[37] Temmler, A., Willenborg, E., and Wissenbach, K., 2011, "Design Surfaces by Laser Remelting," Phys. Procedia, **12**, pp. 419–430.

[38] Ma, C. P., Guan, Y. C., and Zhou, W., 2017, "Laser Polishing of Additive Manufactured Ti Alloys," Opt. Lasers Eng., **93**, pp. 171–177.

[39] Liang, C., Hu, Y., Liu, N., Zou, X., Wang, H., Zhang, X., Fu, Y., and Hu, J., 2020, "Laser Polishing of Ti6Al4V Fabricated by Selective Laser Melting," Metals, **10**(2).

[40] Marimuthu, S., Triantaphyllou, A., Antar, M., Wimpenny, D., Morton, H., and Beard, M., 2015, "Laser Polishing of Selective Laser Melted Components," Int. J. Mach. Tools Manuf., **95**, pp. 97–104.

[41] Grover, T., Pandey, A., Kumari, S. T., Awasthi, A., Singh, B., Dixit, P., Singhal, P., and Saxena, K. K., 2020, "Role of Titanium in Bio Implants and Additive Manufacturing: An Overview," Mater. Today Proc., **26**, pp. 3071–3080.

[42] Kutsukake, A., and Yoshida, Y., 2020, "Influence of Surface Asperity Made by Selective Laser Melting Additive Manufacturing on Bioactivity in Rat Femur," Procedia Manuf., **47**, pp. 1101–1105.

[43] Keaveney, S., Shmeliov, A., Nicolosi, V., and Dowling, D. P., 2020, "Investigation of Process By-Products during the Selective Laser Melting of Ti6AL4V Powder," Addit. Manuf., **36**.

[44] Ahmed Obeidi, M., McCarthy, E., and Brabazon, D., 2016, "Methodology of Laser Processing for Precise Control of Surface Micro-Topology," Surf. Coat. Technol., **307**, pp. 702–712.

[45] Obeidi, M. A., Monu, M., Hughes, C., Bourke, D., Dogu, M. N., Francis, J., Zhang, M., Ahad, I. U., and Brabazon, D., 2021, "Laser Beam Powder Bed Fusion of Nitinol Shape Memory Alloy (SMA)," J. Mater. Res. Technol., **14**, pp. 2554–2570.

[46] Masuo, H., Tanaka, Y., Morokoshi, S., Yagura, H., Uchida, T., Yamamoto, Y., and Murakami, Y., 2018, "Influence of Defects, Surface Roughness and HIP on the Fatigue Strength of Ti-6Al-4V Manufactured by Additive Manufacturing," Int. J. Fatigue, **117**, pp. 163–179.

[47] Pushilina, N., Panin, A., Syrtanov, M., Kashkarov, E., Kudiiarov, V., Perevalova, O., Laptev, R., Lider, A., and Koptyug, A., 2018, "Hydrogen-Induced Phase Transformation and Microstructure Evolution for Ti-6Al-4V Parts Produced by Electron Beam Melting," Metals, **8**(5).

[48] Alberti, C. J., Saito, E., Freitas, F. E. de, Reis, D. A. P., Machado, J. P. B., and Reis, A. G. dos, 2020, "Effect of Etching Temperature on Surface Properties of Ti6Al4V Alloy for Use in Biomedical Applications," Mater. Res., **22**.

[49] Guo, Q., Xie, Y., Wang, X., Lv, S., Hou, T., and Bai, C., 2005, "Synthesis of Uniform Titanium Nitride Nanocrystalline Powders via a Reduction–Hydrogenation–Dehydrogenation–Nitridation Route," J. Am. Ceram. Soc., **88**(1), pp. 249–251.

[50] Zeng, C., Wen, H., Hemmasian Ettefagh, A., Zhang, B., Gao, J., Haghshenas, A., Raush, J. R., and Guo, S. M., 2020, "Laser Nitriding of Titanium Surfaces for Biomedical Applications," Surf. Coat. Technol., **385**.